

stimuli and whose behaviour can be made to self-evolve following the recipes embedded in the DNA sequence. □

Andrea Di Falco is at the School of Physics and Astronomy, University of

St Andrews, St Andrews KY16 9SS, UK.
e-mail: adf10@st-andrews.ac.uk

References

1. Leonhardt, U. *Science* **312**, 1777–1780 (2006).
2. Pendry, J. B., Schurig, D. & Smith, D. R. *Science* **312**, 1780–1782 (2006).

3. Thacker, V. V. *et al. Nature Commun.* **5**, 3448 (2014).
4. Kuzlyk, A. *et al. Nature* **483**, 311–314 (2012).
5. Kuzlyk, A. *et al. Nature Mater.* **13**, 862–866 (2014).
6. Rothmund, P. W. K. *Nature* **440**, 297–302 (2006).
7. Aldaye, F. A., Palmer, A. L. & Sleiman, H. F. *Science* **321**, 1795–1799 (2008).
8. De Luca, A. *et al. ACS Nano* **8**, 2575–2583 (2014).
9. Anderson, P. W. *Science* **177**, 393–396 (1972).

ACOUSTIC METAMATERIALS

Nearly perfect sound absorbers

Membrane-based acoustic resonators of subwavelength dimensions achieve nearly perfect acoustic absorption.

Mathias Fink

Complete sound attenuation by dissipation usually requires thick absorbing materials, with dimensions comparable to the wavelength of low-frequency airborne sound (typically 1–10 m). However, it should be possible to build sound absorbers (or acoustic sinks) that are much smaller than the acoustic wavelength. Such a compact device would be of great interest not only for sound insulation, but could also guide the design of devices that absorb and convert acoustic energy to more useful forms of energy such as electric current. Moreover, a perfect acoustic absorber may also be an elegant solution to overcome the diffraction limit of acoustic waves. This is in fact what Sheng and colleagues report in *Nature Materials*: a nearly perfect acoustic absorber of deep-subwavelength dimensions¹.

To understand the interest and fundamental importance of a subwavelength acoustic sink, one should recall the origin of the diffraction limit in a homogenous medium. The diffraction limit can be understood as the impossibility to focus a perfect spherical converging wave to a single dimensionless focal point. In fact, the diameter of the focal spot, where the

ingoing converging wave of wavelength λ is focused and then transmitted as an outgoing diverging wave, is limited to a minimum dimension of $\lambda/2$. In theory, one way to overcome this fundamental limit is to use a perfect absorber localized at the focal point so as to eliminate the contribution of the outgoing diverging wave to the broadening of the focal spot. Such a perfect absorber would dissipate the energy of the incoming wave and avoid generating any reflected wave. Different strategies have been proposed to build such a perfect absorber. One was demonstrated in the field of elastic waves by using the concept of an active time-reversed source (an active sink) to build an active absorber². However, this approach requires acquiring prior knowledge of the incoming wave, and a set-up to generate the time-reversed source at the focal spot. Other approaches have been proposed in the field of optics by taking advantage of the concept of a perfect coherent absorber³. This is a passive device that relies on the interference of multiple counter-propagating waves within a lossy material to completely dissipate incoming waves while avoiding the generation of any reflected wave (a Fabry–Perot resonator

with matched loss). The drawback of this approach is that it needs a material whose minimal dimension is of the order of $\lambda/2$, thus no longer of subwavelength size.

Sheng and colleagues now show that a decorated membrane resonator (DMR) of deep-subwavelength dimensions — previously used in acoustics to obtain total reflection⁴ — can also be used to achieve total absorption without reflection. A DMR consists of a uniformly stretched elastic membrane decorated by a rigid metallic platelet at its centre (Fig. 1a). Because the membrane's boundary is fixed on a rigid solid frame, the membrane can vibrate at various transverse oscillating modes. Previous work has shown that a DMR embedded in air has two main characteristic frequencies (eigenmodes) — corresponding to the oscillations of the central platelet and the surrounding membrane, and for which there is nearly complete transmission — as well as one so-called anti-resonance frequency, which is sandwiched between the two eigenmode resonances and results in total reflection⁴. Interestingly, when a membrane of sufficiently low elastic modulus is coupled to the platelet mass, the eigenmodes that are obtained correspond to the wavelength of airborne sound (typically two orders of magnitude bigger than the diameter of the membrane resonator, which lies in the centimetre range).

To obtain a regime of total absorption without any reflection, Sheng and co-authors coupled the DMR to a reflecting surface through a thin sealed-gas layer of well-controlled thickness (Fig. 1a). The authors show that such a system forces the two main eigenmodes of the DMR to hybridize and form a new hybrid resonant mode, and that this hybridized mode results in total dissipation at its particular frequency. They also show that by carefully adjusting the thickness of the gas layer it is possible to tune the frequency

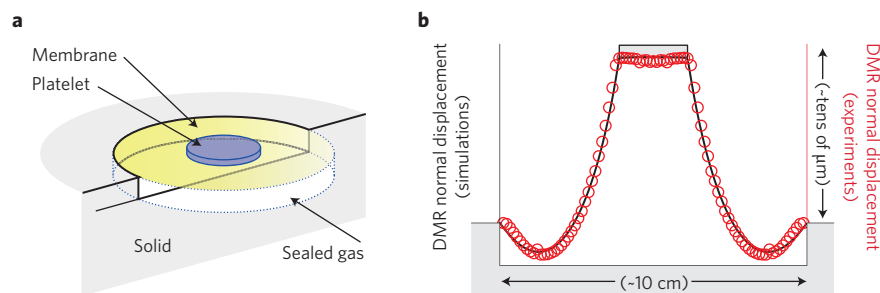


Figure 1 | A nearly perfect acoustic absorber¹. **a**, Schematic of a decorated membrane resonator (DMR). **b**, Normal displacement of the DMR in air at the hybrid resonant mode frequency, resulting from the hybridization of the two main eigenmodes of the DMR (red circles, experimental values; black line, simulated values). Figure adapted from ref. 1, Nature Publishing Group.

of the hybridized mode — and thus its total dissipation effect — to reach perfect matching with the acoustic impedance of air (Fig. 1b). Furthermore, at the hybrid resonant frequency the variance of the membrane's displacement is resonantly amplified. This means that, on resonance, the condition of nearly total absorption is reached: large energy densities are absorbed and dissipated along the lateral dimensions of the weakly lossy membrane; and even when membrane absorption is small enough, the kinetic energy is trapped in

the membrane and efficiently dissipated by viscous means.

Moreover, the authors show that this trapped energy can be transformed into useful electric current, and demonstrate an acoustic-to-electrical energy conversion efficiency of about 23%. Improvements in conversion efficiency can certainly be accomplished, thus opening prospects in energy harvesting. Furthermore, the extension of this concept to multiple frequencies may lead to applications in weak-sound and ultrasound detection. □

*Mathias Fink is at the Institut Langevin at the Ecole Supérieure de Physique et de Chimie de la Ville de Paris, Paris 75005, France.
e-mail: mathias.fink@espci.fr*

References

1. Ma, G., Yang, M., Xiao, S., Yang, Z. & Sheng, P. *Nature Mater.* **13**, 873–878 (2014).
2. de Rosny, J. & Fink, M. *Phys. Rev. Lett.* **89**, 124301 (2002).
3. Wan, W., Chong, Y., Ge, L., Noh, H., Stone, A. D. & Cao, H. *Science* **331**, 889–892 (2011).
4. Yang, Z., Mei, J., Yang, M., Chan, N. H. & Sheng, P. *Phys. Rev. Lett.* **101**, 204301 (2008).

SELF-HEALING POLYMERS

Sticky when wet

Inspired by the chemistry of adhesive proteins in mussels, hydrogels can now be made to self-heal in water without the aid of metal chelates.

Jonathan J. Wilker

Efforts to make synthetic wet-setting adhesives are often foiled by the presence of water. Indeed, the adhesives end up interacting mostly with water rather than bonding to the desired substrate. This difficulty has led scientists to explore how some sea creatures, including mussels¹, oysters² and barnacles³, are able to attach so strongly to wet rocks. Decades of characterization efforts have shown that mussels stick by producing a matrix of proteins containing 3,4-dihydroxyphenylalanine (DOPA)¹, an amino acid made naturally by many plants and animals, and also a neurotransmitter precursor in humans. In recent years, there has been a wave of reports on biomimetic DOPA-based polymers⁴, some of which can even bond more strongly than cyanoacrylates such as commercial Super Glue⁵. Adhesion and crosslinking in these polymers is mediated by the catechol side-chain of DOPA. Similar to the mussels' adhesive system⁶, catechol-containing polymers and hydrogels⁷ can contain an inorganic component (typically Fe³⁺ ions) that through metal chelation — the formation of two or more coordination bonds per metal atom — leads to curing⁶. The reversible and non-covalent nature of metal–ligand bonds is in fact key to the design of self-healing hydrogels⁸. Still, for biomedical applications the toxicity of metals can be a concern. Now, Herbert Waite, Jacob Israelachvili and colleagues report in *Nature Materials* a metal-free approach to the self-healing of polymers in water that relies on hydrogen bonding between catechol moieties⁹.

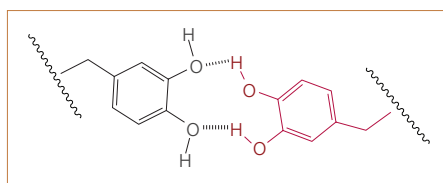


Figure 1 | Bidentate hydrogen bonding between catechol-functionalized polymers mediates polymer self-healing in water.

Using known polymerization chemistry, Waite and co-authors made semi-rigid polyacrylate and more rigid polymethacrylate polymers containing pendant catechols protected with silyl groups. The polymers were cut into two fragments and then rejoined after soaking in acidic (pH 3), neutral (pH 7) or basic (pH 10) aqueous solutions. The acidic medium removed the silyl groups to reveal fully functional catechols, whereas the neutral and basic solutions kept the protecting silyl groups in place. The authors found that self-healing occurred only if deprotected catechols were present at the interface between rejoined fragments, as evidenced by the similar tensile strength of the hydrogel before sectioning and after healing.

When protected, catechols can be hydrogen-bond acceptors; when exposed, however, they are capable of acting both as hydrogen-bond acceptors and donors. Hence, self-healing of the polymers is likely to be driven by hydrogen bonding. The authors' thermodynamic arguments indicate

that hydrogen bonding takes place in a bidentate 1,2-*cis*-diol configuration (Fig. 1). Such an interaction is similar to metal–ligand bonding in that both are non-covalent and able to permit breakage followed by complete reformation. Still, complete consolidation of the self-healing hydrogel seems to occur only after hydrophobic and other weak forces have had a chance to come into play. To provide further evidence for hydrogen bonding, Waite and co-authors performed an experiment in which periodate was used to oxidize the catechol groups to quinones, which cannot be hydrogen-bond donors. Catechol oxidation decreased the adhesive forces between the rejoined fragments of the sectioned hydrogel. Furthermore, the authors used a surface forces apparatus to examine the interfacial bonding between the fragments over time, finding that adhesive forces between exposed catechol polymers exceeded those of the protected analogues, in agreement with the tensile tests. They also noted that forces between fragments surpassed those between the hydrogel and a glass surface.

Moreover, both the adhesive forces and the self-healing ability were larger for the semi-rigid polymer than for the more rigid one. Hence, molecular mobility within the polymer seems to be important. Indeed, self-healing probably involves the peeling apart of bonded pairs of catechols, catechol hydration and repositioning, loss of hydrating water molecules, and the reforming of contacts between catechols. Such processes would be more able to occur when the polymer matrix is softer.

Acoustic metasurface with hybrid resonances

Guancong Ma^{1†}, Min Yang^{1†}, Songwen Xiao¹, Zhiyu Yang¹ and Ping Sheng^{1,2★}

An impedance-matched surface has the property that an incident wave generates no reflection. Here we demonstrate that by using a simple construction, an acoustically reflecting surface can acquire hybrid resonances and becomes impedance-matched to airborne sound at tunable frequencies, such that no reflection is generated. Each resonant cell of the metasurface is deep-subwavelength in all its spatial dimensions, with its thickness less than the peak absorption wavelength by two orders of magnitude. As there can be no transmission, the impedance-matched acoustic wave is hence either completely absorbed at one or multiple frequencies, or converted into other form(s) of energy, such as an electrical current. A high acoustic–electrical energy conversion efficiency of 23% is achieved.

A perfect absorber of deep-subwavelength scale is of great scientific and engineering interest. It can act as the exact time-reversed counterpart of a point source¹, with important implications for time-reversal wave technology^{2,3}. Traditional means of acoustic absorption make use of porous and fibrous materials⁴ and gradient index materials, or employ perforated or micro-perforated panels^{5–7} with tuned cavity depth behind the panels. They generally result in either imperfect impedance matching to the incoming wave, or very bulky structures with dimensions comparable to the wavelength. Space-coiling structures are potentially viable means to reduce the geometric dimensions^{8–10}, but face the challenge of impedance mismatch to the background medium^{8,11}. Active ‘absorbers’, on the other hand, require costly and sophisticated electrical designs¹². Recently, it was shown that, for electromagnetic waves, structuring the interface between two different materials can lead to metasurfaces with diverse functionalities such as phase discontinuity, anomalous refraction/reflection, and polarization manipulation^{13–16}. In particular, the ‘coherent perfect absorber’ (CPA; ref. 17) was realized in optics by relying on phase matching (interference) of counter-propagating waves within a lossy material. Adaptation of the concept to acoustics, however, requires either acoustically thick materials¹⁸, or subwavelength but highly dissipative plates¹⁹ (such as metal for electromagnetic waves), neither of which is practical for low-frequency sound. In addition, all these mechanisms require a specific viscous property or an exact *Q*-factor value to attain optimal absorption performance, making them less robust and difficult to tune.

In this work, we advance the idea of creating two resonances in a thin, weakly absorbing layer with deep-subwavelength transverse dimensions, and then hybridizing the two resonances by placing the layer close to a hard reflecting surface, separated by a thin cell of sealed gas. The hybridized resonance can have two useful degrees of freedom, inherited from the two original resonances, manifested as the average and variance of its (spatially varying) displacement normal to the layer. Whereas the variance component is decoupled from the radiation modes (see below)—that is, deaf—and serves the absorption functionality, the average displacement component can be tuned to impedance-match with the background medium. The net result is a point-like acoustic sink that does not need two counter-propagating waves as in the CPA, and is robust and easy

to fabricate. An acoustic metasurface can be realized as a planar array of such acoustic sinks, with an additional acoustic–electric transducer functionality. Below we present the implementation and theory of this idea, in which the thin layer is a membrane-type acoustic metamaterial.

Decorated membrane resonator

Membrane-type acoustic metamaterials, consisting of decorated membrane resonators (DMRs) of various forms, have been previously studied. It is known that near-complete transmission occurs at the resonant frequencies^{20,21} and de-coupling from the incident wave occurs at so-called anti-resonances, which leads to total reflection^{22–25}. A negative acoustic refraction index can also be realized by using coupled membrane structures²⁶. Also, one can achieve very high acoustic absorption at resonant frequencies through the concentration of curvature energy at the perimeters of asymmetrically shaped platelets²⁷. However, none of the previous studies has anticipated either the phenomenon or the hybrid resonances presented below.

Metasurface unit cell and total absorption

The geometry of a unit cell is illustrated in Fig. 1a. It consists of three parts: a DMR, a reflecting surface, and a thin sealed gas layer in between. The DMR consists of a uniformly stretched elastic membrane with radius $a = 45$ mm and thickness $d \leq 0.2$ mm. It is decorated by a platelet with radius $r = 10$ mm and mass $m = 0.8$ g. The membrane’s boundary is fixed on a rigid frame. The lowest eigenmode of the DMR is characterized by the oscillation of the central platelet at 112 Hz; the second eigenmode at 888 Hz is characterized by oscillation of the surrounding membrane, with the platelet being nearly stationary²² (Fig. 1b). An aluminium back plate as a reflecting surface is separated from the DMR by a gap of depth $s = 17$ mm, sealing a thin layer of gas at atmospheric pressure p . The gas is chosen to be sulphur hexafluoride (SF₆; for its small adiabatic index, see below). We have measured the absorption coefficient for one unit cell of the metasurface, shown in Fig. 2a as a function of frequency. An extremely sharp absorption peak is seen at 152 Hz, with an absorption coefficient > 0.99 , implying a perfect impedance match with air. This is particularly remarkable considering the ultra-small cell thickness $s \approx \lambda/133$, where the wavelength in air $\lambda \approx 2.25$ m at 152 Hz.

¹Department of Physics, Hong Kong University of Science and Technology, Clear Water Bay, Kowloon, Hong Kong, China, ²Institute for Advanced Study, Hong Kong University of Science and Technology, Clear Water Bay, Kowloon, Hong Kong, China. [†]These authors contributed equally to this work.

★e-mail: sheng@ust.hk

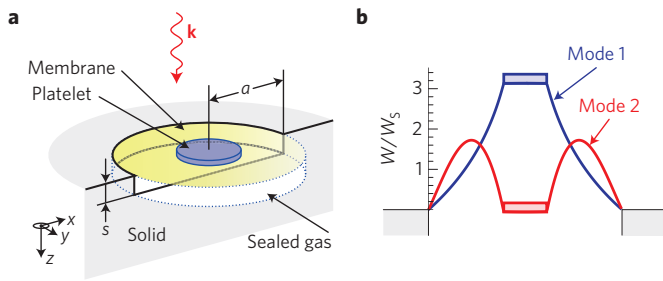


Figure 1 | Geometry and resonance characteristics of the metasurface's unit cell. a, Schematic illustration of the unit cell's components and geometry. Here, a is the radius of the membrane, s is the depth of the sealed gas cell, and \mathbf{k} denotes the incident wavevector. **b**, Schematic cross-sectional illustration of the two lowest frequency eigenmodes of a decorated membrane plotted in reference to the same phase of the incident wave (at the two resonant frequencies), with W being the normal displacement of the membrane, normalized to the incident sound wave amplitude W_s . The flat rectangle at the centre indicates the platelet. The red and blue solid curves denote the membrane.

The extremely small width of the absorption peak, 1.2 Hz, is characteristic of the material's low dissipation coefficient. This sets our absorption mechanism apart from the traditional approach of sound absorption using lossy materials. Surprisingly, the absorption peak coincides with neither eigenfrequency of the DMR, but is located in the vicinity of its anti-resonance. This is shown in Fig. 2a, in which the two arrows mark the frequencies of the first eigenmode and anti-resonance of the DMR. Below we establish that such an extraordinary absorption peak is the consequence of a hybrid resonance.

Hybrid resonance and its characteristics

The gas and reflecting surface effectively add extra impedance in series to the DMR, thereby changing its resonance condition. The above-mentioned DMR eigenmodes are forced to hybridize in the formation of new resonant modes, situated between the previous set of eigenfrequencies. Such hybrid resonances are largely the linear superposition of the two original nearby eigenmodes, and therefore retain their characteristics.

Central to understanding the hybrid modes' behaviour and functionalities is that only the piston-like component of the average membrane displacement, $\langle W \rangle$, couples to transmission and reflection. Here W denotes the normal displacement of the membrane, which is a function of position, as shown in Fig. 1b for the two resonant eigenfunctions, and the angular brackets denote averaging over the area of the membrane. However, the variance of the displacement, defined as $\delta W = \sqrt{\langle (\delta W)^2 \rangle}$, where $\delta W = W - \langle W \rangle$, is decoupled from the radiation modes and hence can be characterized as 'deaf'. The reason for the decoupling can be seen from the Fourier wavevectors \mathbf{k}_\parallel that delineate the lateral spatial pattern of W . For δW , $|\mathbf{k}_\parallel| > 2\pi/\lambda$ necessarily, because $a \ll \lambda$. Owing to the displacement continuity condition and the wave equation, we have $(k_\parallel)^2 + (k_\perp)^2 = (2\pi/\lambda)^2$ for the acoustic wave in air, where k_\perp denotes the wavevector component normal to the membrane. It follows that the δW component of the displacement couples only to the evanescent waves^{24,26}, as its associated k_\perp must be imaginary. In contrast, because the \mathbf{k}_\parallel components for $\langle W \rangle$ have a distribution that peaks at $|\mathbf{k}_\parallel| = 0$, it can couple to the radiation modes—that is, reflection and transmission waves. Hence, if we restrict our considerations to only the radiation modes, then one can treat the problem of our acoustic metasurface as essentially one dimensional in character. The surface impedance, which is required

to match that of air, can be defined using only the $\langle W \rangle$ component, given by $Z = \langle \delta p \rangle / \langle \dot{W} \rangle$, with δp denoting the sound pressure variation and the over-dot denoting the time derivative. Notice that the surface-averaged Green function is defined by $\langle G \rangle = \langle W \rangle / \langle \delta p \rangle$. Hence, for time-harmonic motion with angular frequency ω , we have $Z = (-i\omega \langle G \rangle)^{-1}$.

To explain the emergence of a hybrid resonance and how it matches impedance to the airborne sound, let us first consider the surface-averaged Green function $\langle G_M \rangle$ of the DMR. For simplicity, we consider only the first two lowest frequency eigenmodes W_1 (blue) and W_2 (red) of the DMR shown in Fig. 1b (higher order modes are included in calculations for the data shown in Figs 2 and 4 and for comparison with the experiments), therefore $\langle G_M \rangle$ is given by^{26,28}

$$\langle G_M \rangle = \sum_{i=1}^2 \frac{|\langle W_i \rangle|^2}{\rho_i (\omega_i^2 - \omega^2)} + 2i\beta \sum_{i=1}^2 \frac{|\langle W_i \rangle|^2 \omega}{\rho_i (\omega_i^2 - \omega^2)^2} \quad (1)$$

where $\rho_i \equiv 2\pi d \int_0^a |W_i(r)|^2 \rho(r) r dr$ is a parameter related to the displacement-weighted mass density for the membrane's i th eigenmode, $a = 45$ mm and $d = 0.2$ mm denote the radius and thickness of the membrane, respectively, $\rho(r)$ is the local mass density, and $\omega_1 = 2\pi \times 112$ Hz, $\omega_2 = 2\pi \times 888$ Hz are the relevant angular eigenfrequencies. Equation (1) assumes that the dissipation coefficient β is small, so that the dimensionless $\beta/\omega \ll 1$. The value of β will be determined by fitting to the experiment. The impedance of the DMR is given by $Z_M = (-i\omega \langle G_M \rangle)^{-1}$.

One can locate the anti-resonance frequency of the DMR, $\tilde{\omega} = 2\pi \times 163$ Hz, between the two eigenfrequencies (located by the dashed arrow in Fig. 2a), using the condition $\text{Re} \langle G_M \rangle = 0$. This is obvious because $|Z_M| \rightarrow \infty$ at $\tilde{\omega}$, if the system is without dissipation—that is, $\beta = 0$ —implying decoupling from the incident wave. In anticipation of the fact that the hybrid resonance frequency is always close to $\tilde{\omega}$, we would like to further simplify equation (1) by treating $\Delta\omega = \tilde{\omega} - \omega$ as a small parameter. We denote the derivative of $\text{Re} \langle G_M \rangle$ with respect to frequency, evaluated at $\tilde{\omega}$, as 2Ξ . By expanding it around $\tilde{\omega}$ to the first order in $\Delta\omega$, equation (1) can be simplified to the form $\langle G_M \rangle \simeq 2\Xi(i\beta - \Delta\omega)$, where $\Xi \equiv \sum_{i=1}^2 |\langle W_i \rangle|^2 \tilde{\omega} / [\rho_i (\omega_i^2 - \tilde{\omega}^2)^2]$.

The membrane's two eigenmodes are hybridized by the sealed gas layer, which adds an extra impedance $Z' \equiv \langle \delta p \rangle / \langle \dot{W} \rangle$ to the system. Because the thickness of the sealed gas is orders of magnitude smaller than the relevant wavelength, the sealed gas can be regarded as undergoing uniform adiabatic compression and expansion in response to the membrane's movement, so that we have $\delta p = -\gamma (p/s) \delta s$, where δs denotes variation of the gas layer thickness and γ is the adiabatic index. As $\langle \dot{W} \rangle = -i\omega (-\delta s)$ from the continuity of displacement (positive $\langle W \rangle$ is along the incident wave direction), we obtain $Z' = i\gamma p / (s\omega)$. The total impedance of this stacked system is $Z_h = Z_M + Z'$, so that the Green function of the total system is given by

$$\langle G_h \rangle = (-i\tilde{\omega} Z_h)^{-1} \quad (2)$$

By examining the imaginary part of $\langle G_h \rangle$ in equation (2), it is easy to see that the original resonances at ω_1 and ω_2 are replaced by a new hybridized resonance at ω_h , characterized by the condition $\text{Im} \langle G_h \rangle = 0$, so that

$$\text{Im} \langle G_h \rangle = \frac{1}{\tilde{\omega}} \frac{\text{Re}(Z_M)}{\text{Re}(Z_M)^2 + \text{Im}(Z_h)^2} \quad (3)$$

reaches a peak. A peak in the imaginary part of the Green function signifies a (resonant) mode. Here it is precisely the hybrid resonance as implied by equation (3).

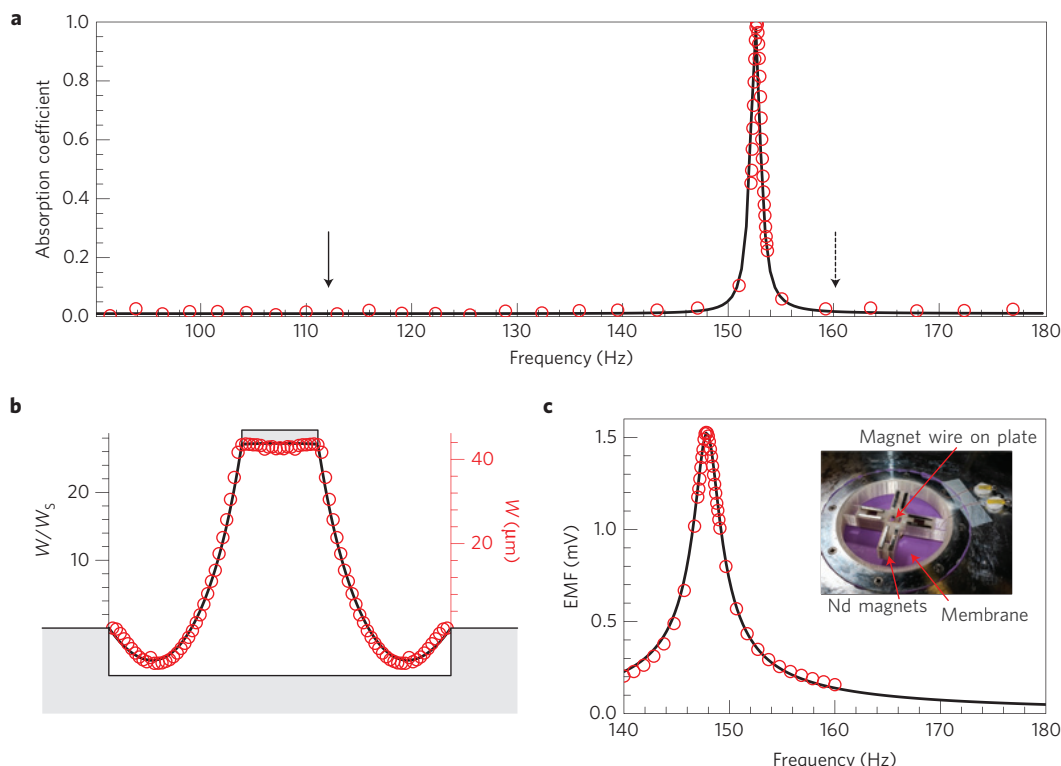


Figure 2 | Manifestations of the hybrid resonance and its energy conversion functionality. **a**, Measured absorption coefficient as a function of frequency. A sharp absorption peak, reaching 0.994, is seen at 152 Hz. The solid and dashed arrows indicate the first eigenmode and anti-resonance of the DMR, respectively. **b**, Normal displacement of the DMR, W (symmetrically plotted from data along the radial direction on one side), at the hybrid resonant absorption peak (152 Hz) is shown in units of the incident wave amplitude, $W_s (=2.5\mu\text{m})$ at an incident sound intensity of 1 Pa. The large amplitude of the hybrid mode is clearly seen by comparing it to Fig. 1b. **c**, Electromotive force (EMF) generated by vibration of the central platelet, with the inset showing the experimental set-up. In this particular case, a power conversion efficiency of 23% is achieved. All experimental results are shown in red circles, and black solid curves denote simulation results. Excellent agreements are seen.

Because the imaginary part of Z_h is zero at the hybrid resonance, it becomes possible to achieve perfect matching with the impedance of air, Z_0 . The relevant conditions are

$$\text{Im}(Z_h/Z_0) = \frac{1}{\bar{s}} - \frac{1}{2\bar{\Xi}} \frac{\Delta\bar{\omega}_h}{\bar{\beta}^2 + \Delta\bar{\omega}_h^2} = 0 \quad (4)$$

$$\text{Re}(Z_h/Z_0) = \frac{1}{2\bar{\Xi}} \frac{\bar{\beta}}{\bar{\beta}^2 + \Delta\bar{\omega}_h^2} = 1 \quad (5)$$

Here $\bar{\Xi} = \Xi/(\bar{\omega}^{-2}Z_0^{-1})$, $\bar{\beta} = \beta/\bar{\omega}$, $\bar{s} = s/(\gamma p Z_0^{-1}\bar{\omega}^{-1})$ and $\Delta\bar{\omega}_h = 1 - \omega_h/\bar{\omega}$ denote the relevant parameters in their dimensionless form. Although the material dissipation coefficient β cannot be easily adjusted, this hybrid impedance-matching condition is still robust as we have two other parameters, \bar{s} and $\Delta\bar{\omega}_h$, which can be easily tuned²² to satisfy equations (4) and (5).

Based on the first four eigenfunctions of the DMR, the evaluated dimensionless $\bar{\Xi} = 0.59$. In Fig. 3a we plot $\bar{\beta}$ (black curve) and \bar{s} (red curve) that satisfy the impedance-matching condition as a function of $\Delta\bar{\omega}_h$. In particular, the value $\Delta\bar{\omega}_h = 0.065$ (indicated by the arrow) corresponds with the observed impedance matching at $\omega_h = 2\pi \times 152$ Hz. One can evaluate the fitted dissipation coefficient $\bar{\beta} = 0.00502$ ($\beta = 5.14$ Hz), and predict the thickness of the SF6 ($\gamma = 1.0984$) gas layer to be $\bar{s} = 0.0772$ ($s = 17.2$ mm). The latter is noted to be in excellent agreement with the experimental value of $s = 17$ mm. We would like to note here that SF6 is chosen in the present experiment for its smaller adiabatic index, which reduces s by $\sim 27\%$ compared to that for air ($\gamma = 1.4$). Furthermore, from the reflection coefficient determined by $R = (Z_0 - Z_h)/(Z_0 + Z_h)$, we can calculate the absorption coefficient as $1 - |R|^2$, plotted as the

black curve in Fig. 2a. Excellent agreement with the experiment is seen.

Dissipation through the deaf component

It may be somewhat surprising that our experimental results indicate that achieving total absorption requires only weak material dissipation (small $\bar{\beta}$). The reason is that the membrane displacement's variance component ΔW , which is deaf, can be very large. When a small absorption coefficient is multiplied by a large energy density, the resulting absorption can still be appreciable. In Fig. 3b we plot the calculated $\Delta W_h/W_s$ as a function of $\Delta\bar{\omega}_h$. In agreement with our expectation, the magnitude of ΔW_h is seen to diverge at $\bar{\omega}(\Delta\bar{\omega}_h = 0)$, at which point both \bar{s} and $\bar{\beta}$ approach zero. This can be understood by realizing that the hybrid mode still retains the characteristics of the two membrane eigenmodes, so that at ω_h (which is close to $\bar{\omega}$) the magnitudes of the amplitudes of the two DMR modes, $\langle W_1 \rangle$ and $\langle W_2 \rangle$, must be comparable—namely, $\langle W_2 \rangle/\langle W_1 \rangle \approx 1$. However, impedance matching implies $\langle W_1 \rangle - \langle W_2 \rangle = \langle W_h \rangle = W_s$. These two conditions can be satisfied only when $\langle W_{1,2} \rangle \gg W_s$, so that $1 - \langle W_2 \rangle/\langle W_1 \rangle = W_s/\langle W_1 \rangle$ is a small number.

To further corroborate the above analysis, we have measured the vibrational profile of the decorated membrane at the total absorption frequency. The experimental result, normalized to 1 Pa (corresponding to 94 dB) of incident sound amplitude, is shown in Fig. 2b as red circles. This hybrid resonance profile is clearly a linear superposition of the membrane's first two eigenmodes. In the same figure we show the numerical simulation results, which are in excellent agreement with the measured profile. From

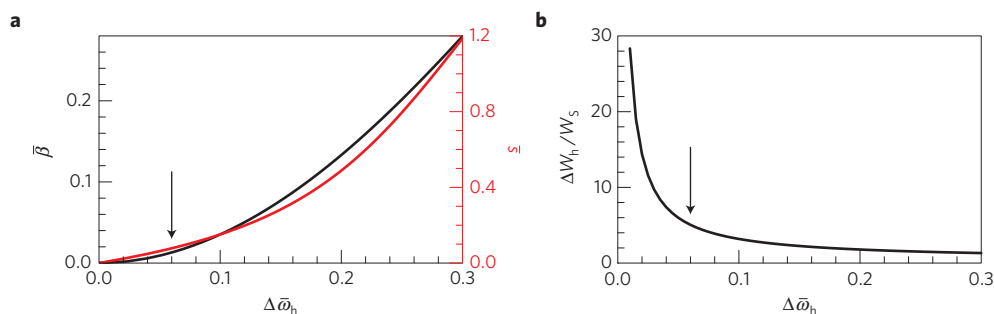


Figure 3 | Relationships between different parameters at the impedance-matched hybrid resonant frequency. **a**, Dimensionless dissipation parameter β (black curve) and dimensionless thickness s (red curve) of the sealed gas layer, plotted as functions of the dimensionless relative frequency location $\Delta\omega_h$ of the hybrid resonance. **b**, Variance of the normal displacement component ΔW_h at the hybrid resonance frequency, plotted as a function of $\Delta\omega_h$. Impedance matching means that the surface-averaged displacement has to be equal to that of the incident sound—that is, $\langle W_h \rangle = \langle W_1 \rangle - \langle W_2 \rangle = W_s$. Proximity to the anti-resonance $\bar{\omega}$ also means that $\langle W_1 \rangle \approx \langle W_2 \rangle$. These two conditions imply a large W_h compared with its surface average, and account for its large variance ΔW_h . In particular, the small dissipation coefficient dovetails with the large W_h in a self-consistent manner so as to achieve total absorption. The arrows in the two figures indicate the parameter values relevant to the experimental results shown in Fig. 2.

the measured displacement, we can evaluate $\langle W_h \rangle \cong 2.8 \mu\text{m}$, which is close to the incident sound amplitude of $W_s = 2.5 \mu\text{m}$ —clear evidence of impedance matching. But $\langle W_h \rangle$ is noted to be one order of magnitude smaller than the maximum displacement of the platelet (over $40 \mu\text{m}$). We can also deduce from the measured data that $\Delta W_h = 5.2 \langle W_h \rangle \cong 14.5 \mu\text{m}$, which is consistent with the relation shown in Fig. 3b (indicated by an arrow). This significantly amplified displacement component near the anti-resonance frequency explains the total absorption functionality for the weakly lossy membrane, and also distinguishes our metasurface from the CPAs: the energy dissipation here is concentrated in the lateral dimensions of the membrane, whereas the CPAs are strictly one dimensional in character, in which waves dissipate as they counter-propagate and interfere along the propagation direction. Here the dissipation coefficient β is small, and it is the very large maximum displacement of the platelet at hybrid resonance that enables the total absorption of the incoming sound. In particular, we wish to demonstrate that such a large displacement also enables the possibility for our metasurface to convert the acoustic energy efficiently to electric current through either piezoelectricity or electromagnetic induction.

Acoustic–electrical power conversion

Acoustic–electrical energy conversion is a topic of intense interest. Applications range from transducers, actuators and sensors, to power scavenging and power transfer. The hybrid mode's impedance-matching capability, in tandem with the confined energy associated with the large ΔW_h , makes the metasurface an excellent candidate for energy conversion. Electromagnetic induction, piezoelectricity and tribo-electrification are commonly used for such tasks. The latter two options require sophisticated micro/nano-fabrication. Here, we choose to demonstrate with a simple inverse-speaker design to extract power. A photo image of the set-up is shown in the inset of Fig. 2c. Magnet wires are supported by a thin plastic frame, which is glued on the central platelet. Four pairs of neodymium magnets are positioned along the magnet wires, generating about 0.6 T of magnetic field perpendicular to both the wires and the direction of platelet's motion. The total length of wires inside the magnetic field is 80 mm. In this simple set-up, the central platelet carries the conductive wire in a large piston-like, up-and-down oscillation, along a direction that is perpendicular to the magnetic field lines. By Faraday's law, we expect an oscillating electric current to be generated in the wires. In this manner acoustic energy is converted into electricity. With a 1 Pa incident sound wave, an electromotive force (EMF) in excess of 1.5 mV was obtained at the hybrid resonance, as shown

in Fig. 2c. The hybrid resonant frequency is slightly lowered to 147 Hz, owing to the $\sim 7.8\%$ extra mass of the conducting wire and other peripherals linked to the central platelet. With a total of 0.6Ω of electric load, the electric power generated is $3.9 \mu\text{W}$, from an incident acoustic power of $17 \mu\text{W}$. The power conversion efficiency is therefore 23%. This efficiency is noted to remain the same for over three orders of magnitude variation in the incident sound intensity (2.5 mPa–4 Pa). Further improvement of the conversion efficiency can be accomplished by a more sophisticated design using stronger magnets and longer wires, in conjunction with better optimized electrical impedance matching with the load.

Total absorption at multiple frequencies

Our metasurface is also capable of unity absorption at multiple frequencies. This is demonstrated by fabricating a metasurface for absorption at multiple frequencies in which each cell comprises three hybrid resonant units. As a result of experimental constraints, all units are reduced to a lateral dimension of $a = 17 \text{ mm}$ and are decorated with $r = 3 \text{ mm}$ platelets, with $m = 0.18 \text{ g}$ for Unit 1, 0.12 g for Unit 2 and 0.06 g for Unit 3, so that each has a different ω_h from the other two. Each unit cell has its own sealed gas cavity, filled with SF₆ at atmospheric pressure. The thickness of the gas layer is 30 mm for Unit 1, 25 mm for Unit 2 and 15 mm for Unit 3. The measured absorption spectra are plotted as a function of frequency in Fig. 4. Total absorption is observed at 255, 309 and 420 Hz. Because the three units face the incident wave in parallel, the total impedance of all three units can be simply calculated in analogy to three parallel impedances in an electrical circuit: $Z_{\text{tot}}^{-1} = Z_1^{-1} + Z_2^{-1} + Z_3^{-1}$. Owing to the very sharp hybrid resonance profile, it is easy to see that $1/Z_i$ must vanish quickly away from $\omega_h^{(i)}$. Therefore, with mismatching resonances, the three units are effectively isolated. It should be noted that the absorption cross-section is almost nine times larger than the geometric cross-section of each unit, owing to the high density of states of each hybrid resonance. Also, because the functionality of the metasurface is based on local hybrid resonances with cells whose lateral dimension is much smaller than the incident sound wavelength, there should be essentially no variation in its characteristics as a function of the incident angle of the sound wave. Hence, the performance of the metasurface, comprising an array of cells each with impedance Z_i , is predictable from the summation of $1/Z_i$.

Conclusions

We report an acoustic metasurface that employs a novel hybrid resonance to achieve robust impedance matching and perfect absorption. The deep-subwavelength scale of its unit cells makes

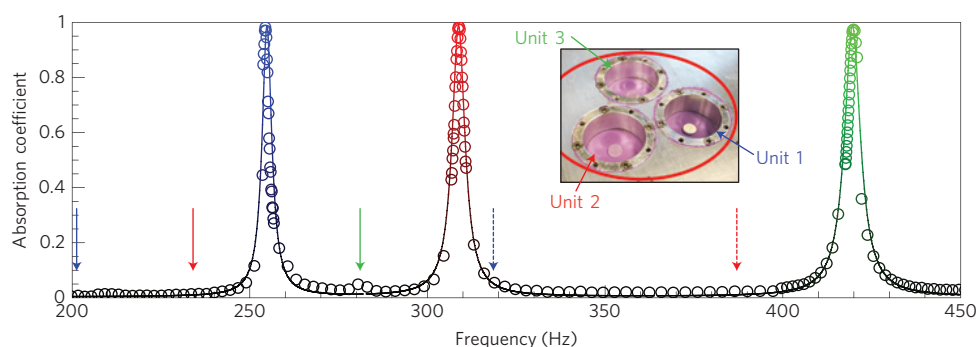


Figure 4 | Unity (>0.99) absorption attained at tunable multiple frequencies. As shown in the inset, three hybrid resonant units are packed closely together. The red circle in the inset depicts the cross-section of the impedance tube. Based on treating the impedances of the three units to be in parallel, theoretical prediction (solid curve) shows excellent agreement with the experiment (open circles). The colour of the circles corresponds with that of the unit label. The solid arrows mark the relevant first eigenfrequencies and the dashed arrows mark the relevant anti-resonances. The anti-resonance frequency for Unit 3 is outside the figure's scale at 514 Hz.

each cell essentially a point acoustic sink, the counterpart to a point source, time-reversed. Its very narrow but tunable total absorption bandwidth may also be advantageous in frequency-selective applications such as filters, sensors and transducers. Extension of the concept to acoustic waves in other fluid media should be straightforward, and may lead to applications in ultrasonics, hydroacoustics and weak sound detection. Its simple construction may also offer considerable potential for applications when combined with existing technologies, such as piezoelectric MEMS^{29,30} and nanowire devices^{31–33}, triboelectric devices^{34,35}, micro-machined transducers^{36,37}, acoustic contactless energy transfer devices^{38,39} and acoustic microscopy⁴⁰.

Methods

Experiments. The bases of metasurfaces are precision-machined from aluminium. Owing to the constraint on the diameter of the impedance tube, the results shown in Fig. 2 are for only one unit cell of the metasurface; for the result shown in Fig. 4, the metasurface consists of three unit cells with reduced lateral dimensions. Measurements of the absorption coefficient were conducted using a modified impedance tube method⁴¹. The impedance tube set-up complies with ASTM C384-04(2011) and ASTM E1050-12: a loudspeaker is mounted on one end of the tube (Brüel & Kjær type-4206), with the metasurface mounted on the other end. Two 1/4-inch condenser microphones (Brüel & Kjær type-4187) are situated at designated positions to sense local pressure. A frequency scan was performed by feeding a sinusoidal signal to a power amplifier and then to the loudspeaker. The outputs of the two microphones were measured using two lock-in amplifiers (Stanford Research SR850) referenced by the same sinusoidal signal. This ensures highly reliable readings of pressure amplitudes and phases at each frequency. The reflection coefficient R can be evaluated from the pressure signals, both the magnitude and phase, gathered from two sensors placed in front of the sample. With the transmission being zero, the absorption coefficient is simply $1 - |R|^2$. Systematic errors in the measurements mainly arise from the finite cross-sectional dimension of the microphones' diaphragms (~4.2 mm in diameter), as the phase of the reflection signal is calculated by assuming the microphone to be a point-like source. In terms of the measured absorption coefficient, the error is negligibly small near the absorption peaks, because the reflection is close to zero. Away from the absorption peak, where the reflection coefficient is close to unity, the maximum error is less than $\pm 2.5\%$, for example, at 180 Hz. The estimated error bar in measurements is smaller than the size of the symbols and hence not shown in Figs 2 and 4.

The normal displacement W was measured by using a laser Doppler vibrometer (Graphtec AT500-05). The vibrometer was mounted on a two-dimensional translational stage so that the surface of the membrane can be scanned. The aluminium back plate was replaced by a piece of optical glass with sufficient thickness such that the system retains hybrid resonance.

Simulations. Numerical simulations were implemented with the 'Acoustic-Solid Interaction Module' in COMSOL Multiphysics v4.2—a commercial finite-element solver software. For eigenstate calculations, a fixed constraint boundary condition was set for the rim of membrane, while the pre-stretching of the membrane was realized by a 0.4 MPa initial stress under geometric nonlinearity. Frequency

domain calculations were used for simulations of the reflection process, where the incident wave was introduced by a plane wave radiation boundary condition. The dissipation was set on the membrane through an isotropic structural loss factor.

Received 22 December 2013; accepted 25 April 2014;
published online 1 June 2014

References

- De Rosny, J. & Fink, M. Overcoming the diffraction limit in wave physics using a time-reversal mirror and a novel acoustic sink. *Phys. Rev. Lett.* **89**, 124301 (2002).
- Derode, A., Roux, P. & Fink, M. Robust acoustic time reversal with high-order multiple scattering. *Phys. Rev. Lett.* **75**, 4206–4209 (1995).
- Fink, M. Time reversed acoustics. *Phys. Today* **50**, 34–40 (March, 1997).
- Arenas, J. P. & Crocker, M. J. Recent trends in porous sound-absorbing materials. *J. Sound Vib.* **44**, 12–18 (2010).
- Maa, D.-Y. Potential of microperforated panel absorber. *J. Acoust. Soc. Am.* **104**, 2861 (1998).
- Fuchs, H. V. & Zha, X. Micro-perforated structures as sound absorbers—a review and outlook. *Acta. Acust. United Acc.* **92**, 139–146 (2006).
- Maa, D.-Y. Practical single MPP absorber. *Int. J. Acoust. Vib.* **12**, 3–6 (2007).
- Liang, Z. & Li, J. Extreme acoustic metamaterial by coiling up space. *Phys. Rev. Lett.* **108**, 114301 (2012).
- Liang, Z. *et al.* Space-coiling metamaterials with double negativity and conical dispersion. *Sci. Rep.* **3**, 1614 (2013).
- Xie, Y., Popa, B.-I., Zigoneanu, L. & Cummer, S. A. Measurement of a broadband negative index with space-coiling acoustic metamaterials. *Phys. Rev. Lett.* **110**, 175501 (2013).
- Xie, Y., Konneker, A., Popa, B.-I. & Cummer, S. A. Tapered labyrinthine acoustic metamaterials for broadband impedance matching. *Appl. Phys. Lett.* **103**, 201906 (2013).
- Scheuren, J. *Handbook of Engineering Acoustics* 301–334 (Springer, 2013).
- Yu, N. *et al.* Light propagation with phase discontinuities: Generalized laws of reflection and refraction. *Science* **334**, 333–337 (2011).
- Ni, X., Emani, N. K., Kildishev, A. V., Boltasseva, A. & Shalaev, V. M. Broadband light bending with plasmonic nanoantennas. *Science* **335**, 427 (2012).
- Kildishev, A. V., Boltasseva, A. & Shalaev, V. M. Planar photonics with metasurfaces. *Science* **339**, 1232009 (2013).
- Yin, X., Ye, Z., Rho, J., Wang, Y. & Zhang, X. Photonic spin Hall effect at metasurfaces. *Science* **339**, 1405–1407 (2013).
- Chong, Y., Ge, L., Cao, H. & Stone, A. D. Coherent perfect absorbers: Time-reversed lasers. *Phys. Rev. Lett.* **105**, 053901 (2010).
- Wan, W. *et al.* Time-reversed lasing and interferometric control of absorption. *Science* **331**, 889–892 (2011).
- Pu, M. *et al.* Ultrathin broadband nearly perfect absorber with symmetrical coherent illumination. *Opt. Express* **20**, 2246–2254 (2012).
- Park, J. J., Lee, K. J. B., Wright, O. B., Jung, M. K. & Lee, S. H. Giant acoustic concentration by extraordinary transmission in zero-mass metamaterials. *Phys. Rev. Lett.* **110**, 244302 (2013).
- Fleury, R. & Alù, A. Extraordinary sound transmission through density-near-zero ultranarrow channels. *Phys. Rev. Lett.* **111**, 055501 (2013).

22. Yang, Z., Mei, J., Yang, M., Chan, N. H. & Sheng, P. Membrane-type acoustic metamaterial with negative dynamic mass. *Phys. Rev. Lett.* **101**, 204301 (2008).
23. Yang, Z., Dai, H., Chan, N., Ma, G. & Sheng, P. Acoustic metamaterial panels for sound attenuation in the 50–1000 Hz regime. *Appl. Phys. Lett.* **96**, 041906 (2010).
24. Mei, J., Ma, G., Yang, M., Yang, J. & Sheng, P. *Dynamic Mass Density and Acoustic Metamaterials. Acoustic Metamaterials and Phononic Crystals* (Springer, 2013).
25. Ma, G., Yang, M., Yang, Z. & Sheng, P. Low-frequency narrow-band acoustic filter with large orifice. *Appl. Phys. Lett.* **103**, 011903 (2013).
26. Yang, M., Ma, G., Yang, Z. & Sheng, P. Coupled membranes with doubly negative mass density and bulk modulus. *Phys. Rev. Lett.* **110**, 134301 (2013).
27. Mei, J. *et al.* Dark acoustic metamaterials as super absorbers for low-frequency sound. *Nature Commun.* **3**, 756 (2012).
28. Yang, M., Ma, G., Wu, Y., Yang, Z. & Sheng, P. Homogenization scheme for acoustic metamaterials. *Phys. Rev. B* **89**, 064309 (2014).
29. Horowitz, S. B. & Sheplak, M. Aeroacoustic applications of acoustic energy harvesting. *J. Acoust. Soc. Am.* **134**, 4155 (2013).
30. Horowitz, S. B., Sheplak, M., Cattafesta, L. N. III & Nishida, T. A MEMS acoustic energy harvester. *J. Micromech. Microeng.* **16**, S174–S181 (2006).
31. Cha, S. N. *et al.* Sound-driven piezoelectric nanowirebased nanogenerators. *Adv. Mater.* **22**, 4726–4730 (2010).
32. Qin, Y., Wang, X. & Wang, Z. L. Microfibre–nanowire hybrid structure for energy scavenging. *Nature* **451**, 809–813 (2008).
33. Wang, X., Song, J., Liu, J. & Wang, Z. L. Direct-current nanogenerator driven by ultrasonic waves. *Science* **316**, 102–105 (2007).
34. Fan, F.-R., Tian, Z.-Q. & Wang, Z. L. Flexible triboelectric generator. *Nano Energ.* **1**, 328–334 (2012).
35. Zhu, G. *et al.* Toward large-scale energy harvesting by a nanoparticle-enhanced triboelectric nanogenerator. *Nano Lett.* **13**, 847–853 (2013).
36. Ladabaum, I., Jin, X., Soh, H. T., Atalar, A. & Khuri-Yakub, B. T. Surface micromachined capacitive ultrasonic transducers. *IEEE. Trans. Ultrason. Ferroelectr. Freq. Control* **45**, 678–690 (1998).
37. Ergun, A. S., Yaralioglu, G. G. & Khuri-Yakub, B. T. Capacitive micromachined ultrasonic transducers: Theory and technology. *J. Aerospace Eng.* **16**, 76–84 (2003).
38. Roes, M., Hendrix, M. & Duarte, J. *IECON 2011–37th Annual Conference on IEEE Industrial Electronics Society* 1238–1243 (2011).
39. Shmilovitz, D., Ozeri, S., Wang, C. & Spivak, B. Noninvasive control of the implant power for an ultrasonic transcutaneous energy transfer device. *IEEE Trans. Biomed. Eng.* **61**, 995–1004 (2013).
40. Fox, J. D., Kino, G. S. & Khuri-Yakub, B. T. Acoustic microscopy in air at 2 MHz. *Appl. Phys. Lett.* **47**, 465–467 (1985).
41. Ho, K. M., Yang, Z., Zhang, X. X. & Sheng, P. Measurements of sound transmission through panels of locally resonant materials between impedance tubes. *Appl. Acoust.* **66**, 751–765 (2005).

Acknowledgements

P.S. and M.Y. wish to thank Ying Wu and Jun Mei for helpful discussions. This work is supported by AoE/P-02/12 and HKUST2/CRF/11G.

Author contributions

P.S. initiated, designed and supervised the project. M.Y. and P.S. provided the theoretical framework. G.M. designed and carried out the experiments. S.X. assisted with the experiments. M.Y. carried out the numerical simulations. G.M., M.Y., Z.Y. and P.S. analysed the data. G.M., M.Y. and P.S. wrote the manuscript.

Additional information

Reprints and permissions information is available online at www.nature.com/reprints. Correspondence and requests for materials should be addressed to P.S.

Competing financial interests

The authors declare no competing financial interests.